




High-resolution transmission electron microscopy study of body-centered tetragonal Zr₂Fe nanoparticle phase in Zircaloy-4 alloy and its typical crystalline defect structures

Fuzhou Han^{1,2}, Fusen Yuan^{1,2}, Geping Li^{1,2,*} , Yingdong Zhang^{1,2}, Wenbin Guo^{1,2}, Muhammad Ali^{1,2}, Jie Ren^{1,2}, Chengze Liu^{1,2}, Hengfei Gu^{2,3}, and Gaihuan Yuan⁴

¹ School of Materials Science and Engineering, University of Science and Technology of China, 72 Wenhua Road, Shenyang 110016, People's Republic of China

² Shi-Changxu Innovation Center for Advanced Materials, Institute of Metal Research, Chinese Academy of Sciences, 72 Wenhua Road, Shenyang 110016, People's Republic of China

³ University of Chinese Academy of Sciences, 19 Yuquan Road, Beijing 100049, People's Republic of China

⁴ State Nuclear Bao Ti Zirconium Industry Company, Baoji 721013, People's Republic of China

Received: 19 May 2021

Accepted: 8 August 2021

Published online:

19 August 2021

© The Author(s), under exclusive licence to Springer Science+Business Media, LLC, part of Springer Nature 2021

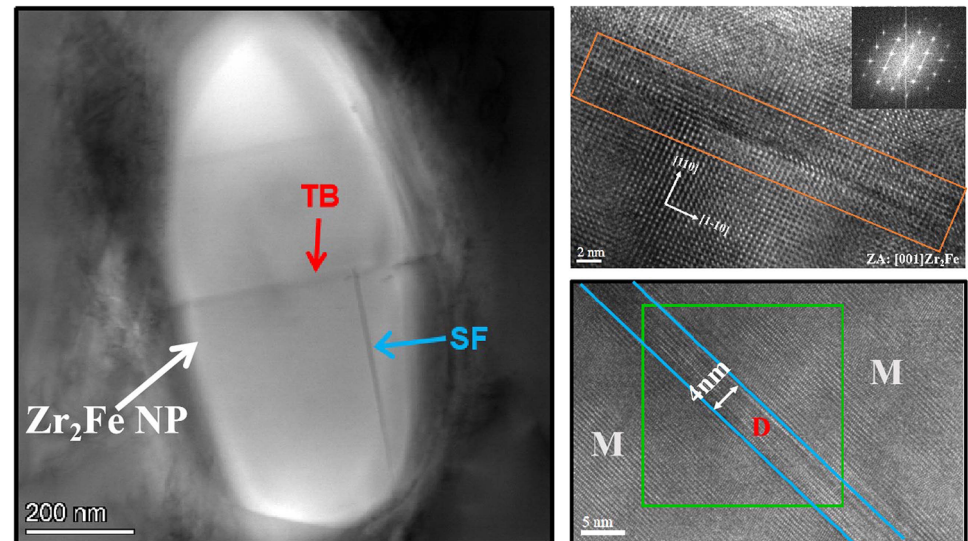
ABSTRACT

Transmission electron microscopy (TEM) and energy-dispersive X-ray spectroscopy have been employed for crystallographic and microstructural characterization of nano-precipitates distributed within the α -Zr matrix of the Zircaloy-4 (Zr-4) alloy. These nano-precipitates, typically with an average length between 200 and 500 nm, have been identified as the C16-type Zr₂Fe phase. A massive presence of randomly distributed planar defects, including stacking faults and sub-unit cell twins, were detected. Atomic-scale configurations of the intrinsic planar defects in the Zr₂Fe nanoparticle phase were investigated, for the first time, through high-resolution TEM analysis. Results show that the stacking faults are extended on (110) planes with a displacement vector of $1/4[1\bar{1}1]$. HRTEM observations and electron diffraction patterns acquired by specimen tilting reveal that these twin defects belong to 60° rotation twin with the rotation axis along the [110] direction. Geometric analysis based on the the TEM results reveals that the twinning plane and direction are $1\bar{1}2$ and $[3\bar{3}2]$.

Handling Editor: N. Ravishankar.

Address correspondence to E-mail: gpli@imr.ac.cn

GRAPHICAL ABSTRACT



Introduction

Nuclear energy has been increasingly developed in major nuclear power nations around the world as an efficient basic and clean energy source without any carbon emissions. Zirconium alloys present low thermal neutron absorption cross-section together with excellent mechanical properties and good resistance to corrosion in high-temperature water, making them suitable for application in the nuclear reactor core as the fuel cladding tubes and structure materials [1–3]. Zircaloy-4 (Zr-4) alloy is the most widely used one among all zirconium alloys due to its combined mechanical properties and good resistance to corrosion [4, 5]. The principal alloying elements in Zr-4 alloy including tin, iron, and chromium, are generally present in the form of intermetallic phases (also known as secondary phase precipitates, SPPs) due to the limited solubility of Fe and Cr in α -zirconium. Laves phases with AB₂ stoichiometry that can exist with three different crystal structures including cubic C15 (3C), hexagonal C14 (2H), and dihexagonal C36 (4H) structures, are the most frequently observed intermetallic phase in the Zr–Sn alloys [6–11]. However, based on our transmission electron microscopy (TEM) analyses results,

the intermetallic nano-precipitates in the Zr-4 alloy have been identified as C16-type Zr₂Fe phase with a body-centered tetragonal (BCT) structure, which is isomorphous with the CuAl₂.

In the Fe–Zr phase diagram proposed by Jiang [12], the Zr₂Fe equilibrium phase was reported to have a tetragonal structure at a composition of approximately 67% at Zr. As a part of a group, intermetallic compounds isostructural with CuAl₂, Zr₂Fe phase has also been reported in some systems of binary and ternary alloys [13–17]. However, there is little information about the crystallography of Zr₂Fe phase at the atomic scale, although this precipitates phase has been reported several times. Furthermore, to our knowledge, the atomic details of the associated defect structures remain essentially unknown. In the view of nano-precipitates (NPs) and inside defects, which significantly affect the corrosion resistance and mechanical properties of zirconium alloys [18, 19], an accurate knowledge of the microstructural characterization of these SPP is of great importance for a better understanding of the structure–property relationship and designing materials with improved properties.

In the present study, TEM observation has been performed to study the Zr₂Fe phase precipitated in

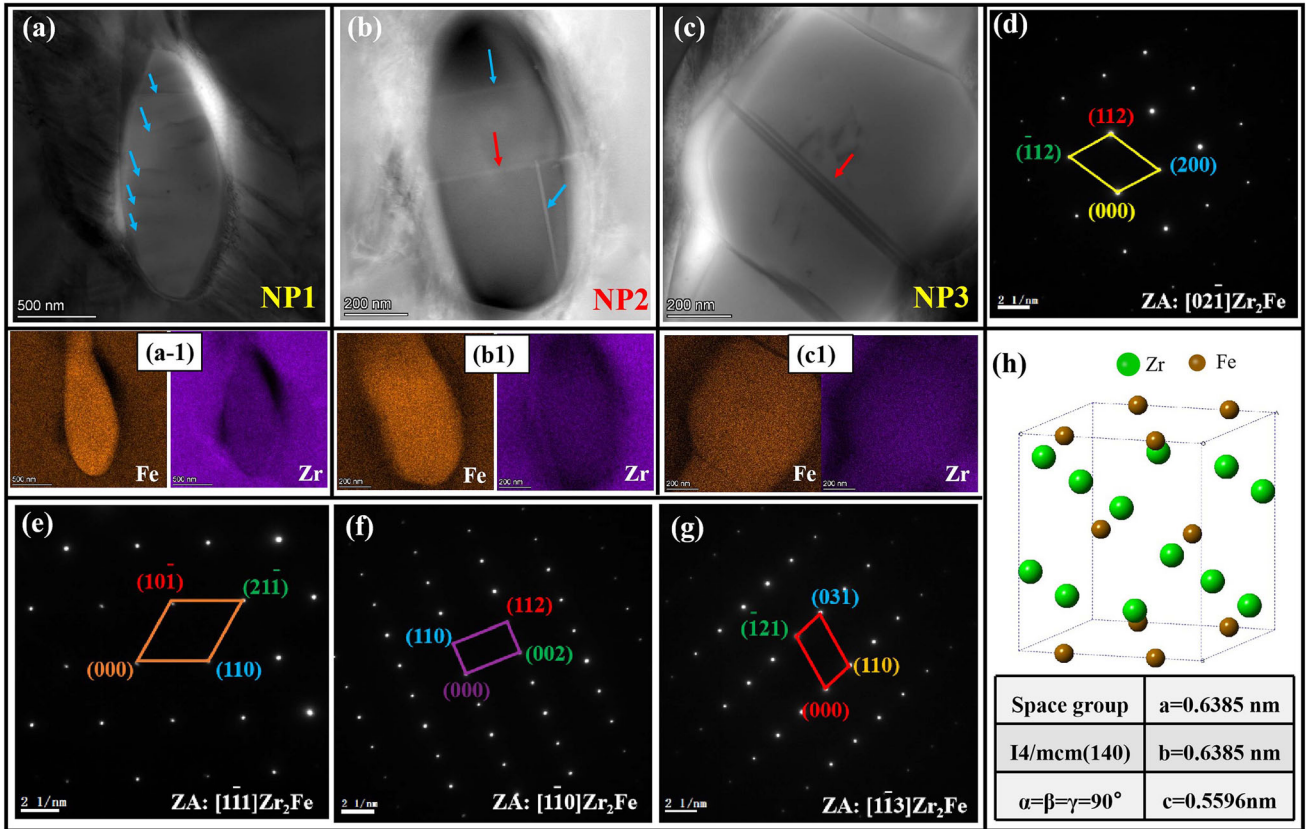
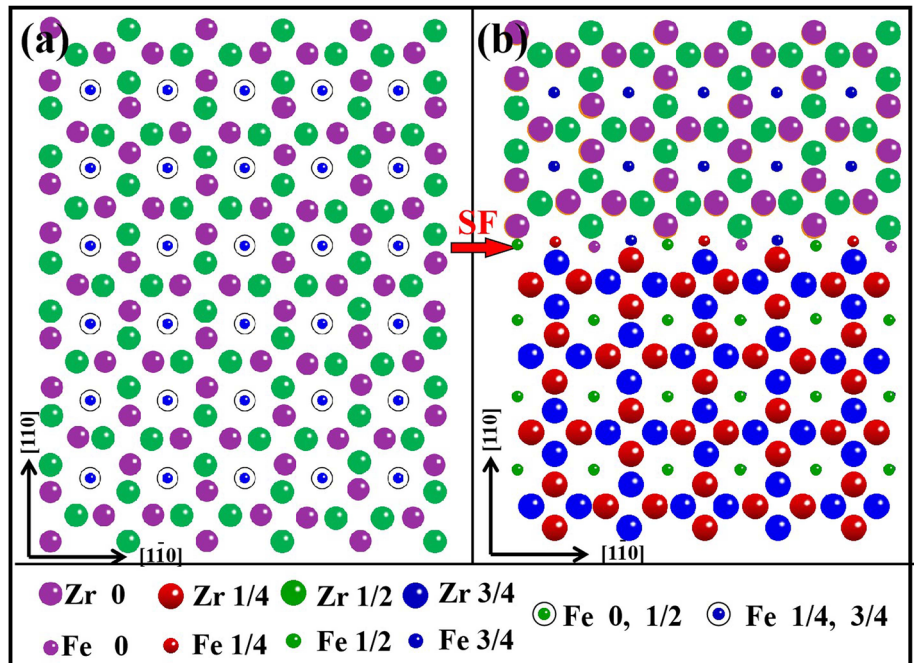


Figure 1 STEM images, EDS mapping and corresponding SAED patterns of Zr_2Fe , observed in Zr-4 alloy. **a–c** Scanning transmission electron microscopy (STEM) images show the NPs and corresponding EDS mapping **d–g** A series of indexed SAED

patterns obtained from the NPs along with different crystallographic directions. **h** Three-dimensional view of the Zr_2Fe unit cell and the measured lattice parameters.

Figure 2 **a** Atomic model of a perfect Zr_2Fe crystal viewed along $[001]$ direction **b** with an intrinsic stacking fault (SF). The crystallographic directions and SF are denoted by black and red arrows, respectively.



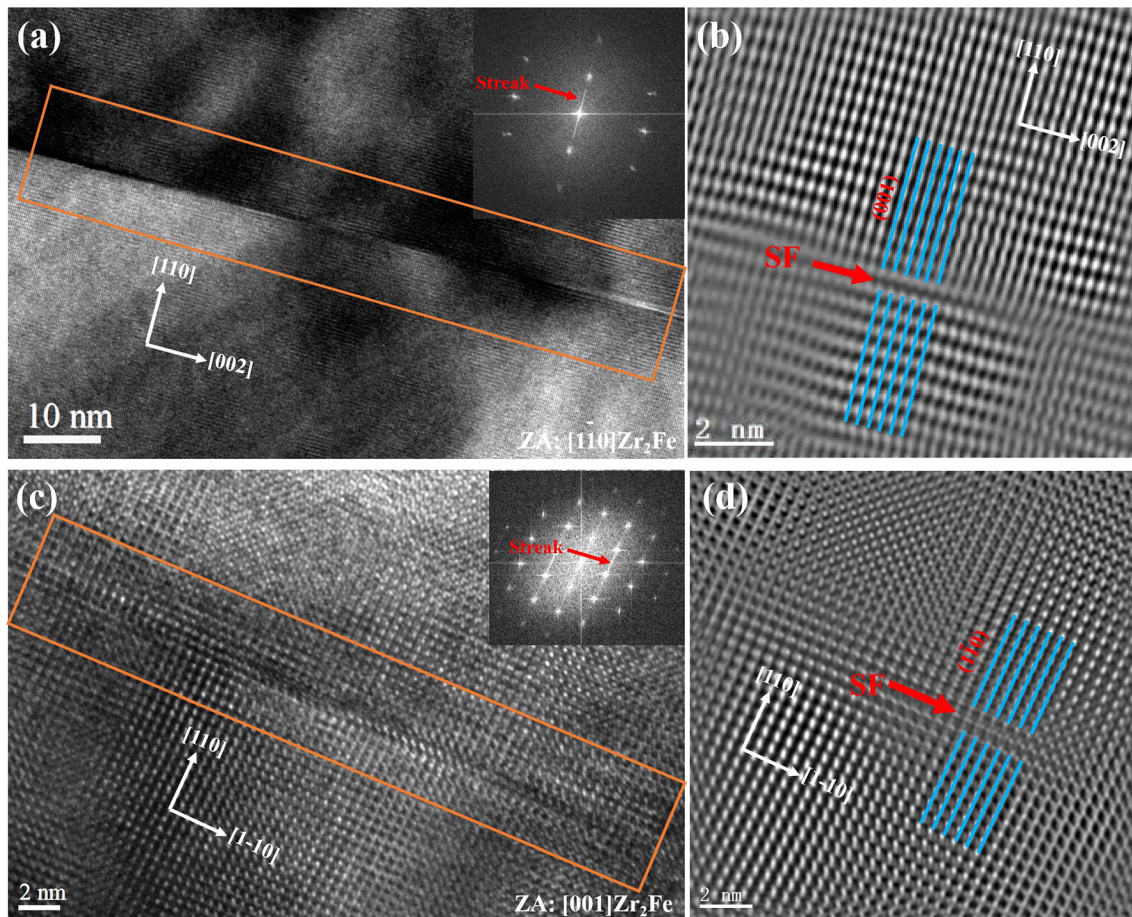


Figure 3 HRTEM micrographs of two Zr_2Fe NPs viewed respectively along with **a** $[1\bar{1}0]$ and **c** $[001]$ crystallographic directions, with stacking faults marked by rectangles. **b** and **d** are

the corresponding enlarged HRTEM filtered images showing the displacement vectors components. The crystallographic directions and stacking faults are indicated in the figures.

Zr-4 alloy and special attention was devoted to characterize the defect structures by high-resolution TEM (HRTEM). The aim is to provide insights into this type of intermetallic compound and benefit the design of new zirconium alloys.

Material and experimental procedures

Zr-4 alloy ingots used in the present study were prepared by arc-melting on a water-cooled copper crucible under a protective argon atmosphere. The chemical composition of the as-cast ingots measured by optical emission spectrometry was Zr-1.45Sn-0.20Fe-0.12Cr (wt.%). The ingots were then sealed into quartz tubes under vacuum condition and subjected to the solution treatment at 1200 °C for 8 h, followed by furnace cooling to room temperature. Slices with dimensions of 12 mm × 10 mm × 1 mm

were cut from the ingots along the radial direction. These slices were first mechanically ground to ~ 60 μm in thickness, then several disks with a diameter of 3 mm were punched from each slice. Subsequently, by using Struers Tenupol-5 twin-jet electron polisher, thinning perforation was carried out with a solution of 10% perchloric acid and 90% ethanol in volume fraction, at - 30 °C under an applied voltage of 20 V. With the combined use of bright-field scanning transmission electron microscopy (STEM) imaging, energy dispersive spectrometer (EDS), and high-resolution TEM (HRTEM), systematic investigations on these precipitates were performed on a JEM 2100F transmission electron microscopy at standard acceleration voltage of 200 kV.

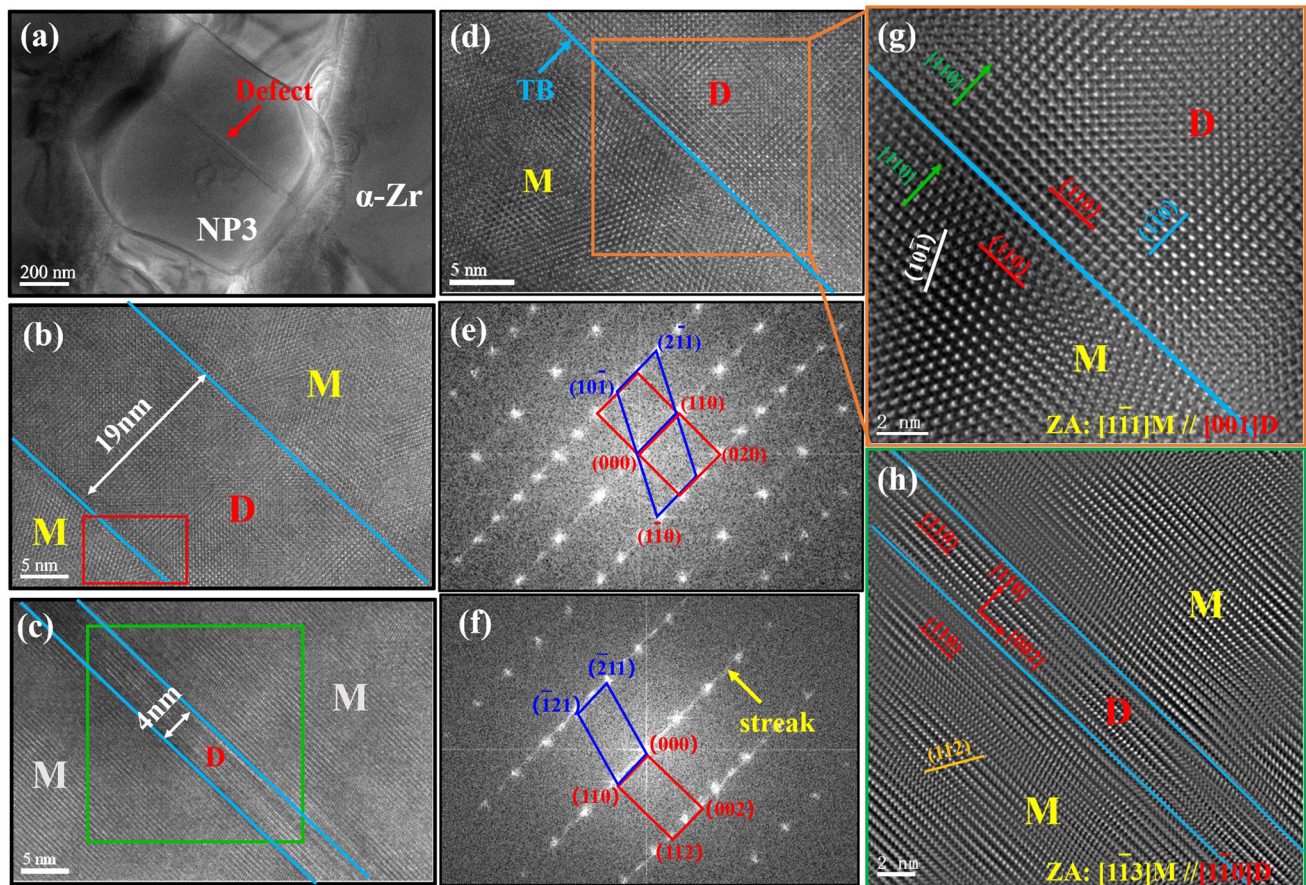


Figure 4 **a** Bright-Field TEM (BF TEM) image of the faulted NP₃. **b** and **c** are HRTEM images showing the contained defects in the NP₃ along $[1\bar{1}1]$ and $[1\bar{1}3]$ directions, respectively **d** Enlarge HRTEM micrograph of the left defect-matrix boundary in Fig. 4b, as indicated by red rectangle **e** and **f** are FFT patterns transformed

correspondingly from Fig. 4b and c, respectively **g** and **h** are Fourier filtered HRTEM images captured from the framed regions in Fig. 4c and d. Note that the letters ‘M’ and ‘D’ are respectively refer to Zr₂Fe matrix and its contained defect.

Results and discussion

As shown in Fig. 1a–c, NPs (as indicated by yellow arrows in Fig. 1a–c) with massive shapes and equivalent diameters ranging from 200 to 500 nm were generally observed in the Zr-4 alloy. STEM observations show that one or more straight lines (as indicated by blue and red arrows) with dark contrast terminating at the grain or transverse the whole NP were observed within the parts of NPs, which are hereinafter together referred to as the defect. EDS analysis indicates that these NPs were enriched by Fe (see the elemental mapping of the NPs in Fig. 1) and can be identified as C16-type Zr₂Fe particles with a CuAl₂-type body-centered tetragonal structure according to the series of selected area electron diffraction (SAED) patterns along, and $[001]$, $[1\bar{1}3]$

$[1\bar{1}0]$ and $[1\bar{1}1]$ zone axes. The space group and refined lattice parameters are present in Fig. 1h.

Although defect structures in the C16-type Zr₂Fe have rarely been detected, crystals with similar structures have been widely reported and investigated. The most complete slip systems in crystals with such body-centered tetragonal (BCT) structure were recognized as $(110)\langle 001 \rangle$, $(010)\langle 001 \rangle$, $(310)\langle 001 \rangle$, $(010)\langle 100 \rangle$, $110\langle 1\bar{1}0 \rangle$, $(112)1/2\langle 1\bar{1}1 \rangle$ and $(112)1/2\langle \bar{1}\bar{1}1 \rangle$ [20–22]. Based on the BCT crystal structure [22–24], an atomic model for the occurrence of an intrinsic stacking fault can be constructed as shown in Fig. 2, in which stacking faults are generated through the shearing of atoms on (110) plane with a displacement vector of $a/4[111]$ in the perfect crystal, as shown in Fig. 2b.

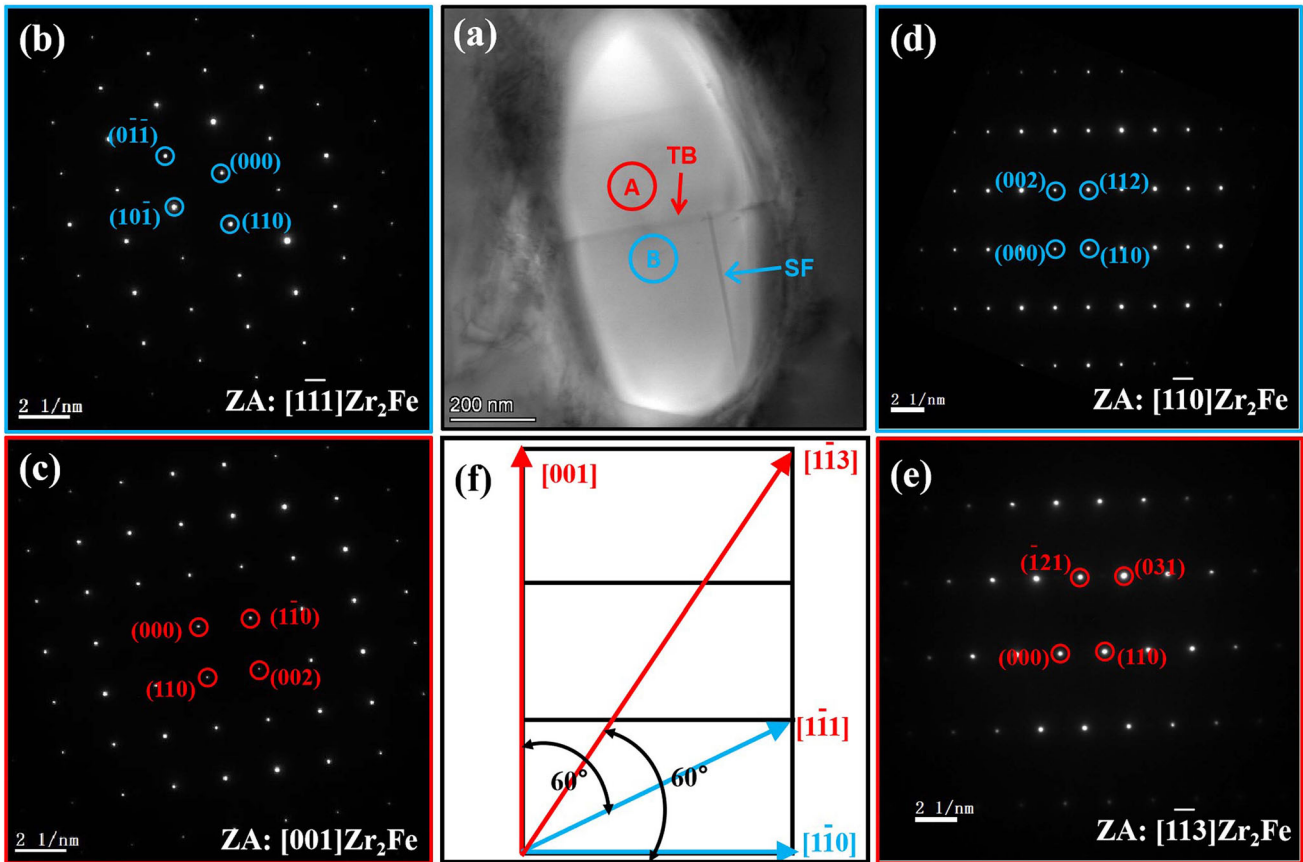


Figure 5 **a** STEM image showing defects within the Zr_2Fe NP2. **b** and **c** are electron diffraction patterns (EDPs) captured from above and below parts (as indicated by red and blue circles) at the

same tilting condition, indexed as $[1\bar{1}1]$ and $[001]$, respectively. **d** and **e** are corresponding EDPs obtained at another TEM tilting condition, indexed as $[1\bar{1}0]$ and $[1\bar{1}3]$.

Figure 3a, c are HRTEM images of the stacking faults typically observed within Zr_2Fe recorded with the incident electron beam parallel to $[1\bar{1}0]$ and $[001]$ crystallographic directions, respectively. It is evident that stacking faults (as marked by orange rectangles) with gray contrast streaks running parallel to (110) planes can indeed be seen. The corresponding fast fourier transformation (FFT) pattern captured from the faulted zone, as shown in the illustration in Fig. 3a, shows order arrange diffraction spots accompanied by diffuse intensity streaks along $[110]$ reciprocal vector, owing to the presence of (110) planar defects inside the precipitates. The stacking fault has never been reported in Zr_2Fe phase before to our knowledge. The in-plane rigid body component of the stacking fault can be easily estimated from Fig. 3b, an inverse fast fourier transformation (IFFT) image of the faulted region in Fig. 3a along $[1\bar{1}0]$ the direction. At a close inspection of Fig. 3b, the white spots in the upper and lower parts of the stacking

faults region were displaced parallel to the (110) plane (blue lines). In the present observation, multi-slice simulations show that the white dots represent a large tunnel between the atomic columns, repeating periodicities $1/2[001]$ and $1/2[110]$. Therefore, in the $[110]$ direction, two consecutive white dots are separated by $a/\sqrt{2} = 0.45$ nm. The fringe shifts along the fault plane are close or equal to half a period, i.e., the displacement vector fraction is $1/4[001]$ measured in the $[1\bar{1}0]$ projection. Figure 3d shows the IFFT image of another stacking fault along $[001]$ the crystallographic direction, corresponding to the faulted regions in Fig. 3c. The displacements of the atomic columns along the fault planes are similar, close, or equal to half a period, i.e., have an in-plane component $1/4[110]$. Because the HRTEM observations of stacking faults are carried out along two mutually vertical crystallographic directions ($[1\bar{1}0]$ and $[001]$ directions) of Zr_2Fe NP phase, therefore, the three-

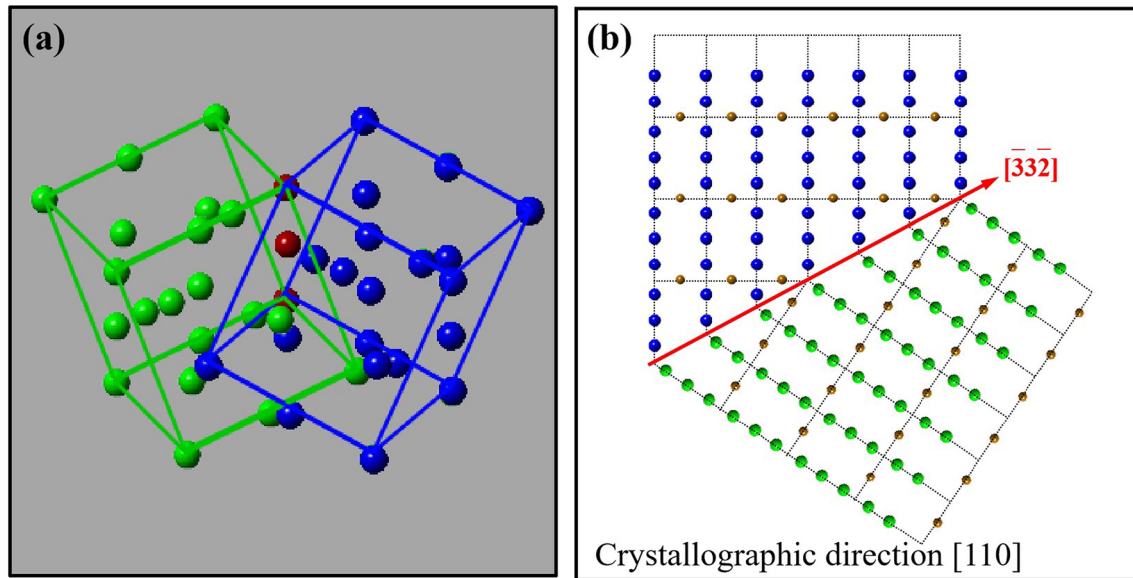


Figure 6 **a** Schematic diagram shows the orientation of twins and Zr_2Fe matrix phase, in which the green and blue crystal lattices stand for matrix and rotation twin, respectively. The red atoms are

shared by twin and Zr_2Fe phase matrix **b** Atom model simulation shows the crystallographic relation of the rotation twin and Zr_2Fe nano-precipitate phase viewed from the $[110]$ direction.

dimensional displacement vector of stacking faults is $1/4[1\bar{1}1] = 1/4[001] + 1/4[1\bar{1}0]$ for Zr_2Fe phase, which agrees well with the crystallographic consideration in crystals with BCT structure[22–24].

Figure 4a shows a bright-field TEM (BF TEM) image of the faulted Zr_2Fe NP₃. It can be clearly seen that this NP contains obviously transverse streaks (as denoted by red arrow), which correspond to the defects observed under STEM observation. Different from the above-mentioned stacking faults, this planar defect penetrates through the whole grain of Zr_2Fe and leaves a clear boundary. Figure 4b, and c are high-resolution transmission electron microscopy (HRTEM) images showing the contained defects along different crystallographic directions. Figure 4d displays an enlarged HRTEM microscopy of the left boundary between defect and matrix in Fig. 4b. The thickness of defects present in Fig. 4b, c were measured to be 19 nm and 4 nm, respectively. And the atomic stacking sequence in Zr_2Fe matrix phase is obviously different from that of the defect. By analysis of the corresponding FFT patterns in Fig. 4e, f, it can be deduced that the orientation relationship between the matrix and the defect can be deduced as $(110)_M // (110)_D$ and $[1\bar{1}1]_M // [001]_D, [1\bar{1}3]_M // [1\bar{1}0]_D$. Enlarged HRTEM images of matrix-twin boundaries are shown in Fig. 4g, h, which also reveals that (110) the plane was shared by defect and matrix.

Figure 5a is a bright-field image of NP₂ showing clear transverse twin defect formed in the Zr_2Fe grain (as denoted by red arrow). The Zr_2Fe NP₂ grain can be divided into two regions (the upper and below parts) by the twin boundary. Figure 5b, d shows the EDPs obtained from the below part (as marked with blue circle in Fig. 5a) while Fig. 5c, e are the corresponding EDPs obtained from the upper part (as shown in red circle in Fig. 5a) at the same tilting conditions as Fig. 5c, d, respectively. It is evident that all the diffraction patterns contain (110) plane, suggesting that the defect was accomplished by a rotation along the matrix $[110]$ crystallographic axis. Figure 5f shows the schematic of the crystallographic relationships between these zone axes, in which the angles between $[1\bar{1}1]$ and $[001]$, $[1\bar{1}0]$ and $[1\bar{1}3]$ are all nearly 60° . Therefore, these defects can be recorded as 60° rotation twins along the $[110]$ crystallographic axis [23–26].

In order to determine the crystallography between Zr_2Fe phase and its contained twin defect structure, three-dimensional unit cells based on the TEM results was constructed base on the TEM results, as shown in Fig. 6a. The blue and yellow frameworks were referred to as the unit cells of the Zr_2Fe and twin, respectively. The twinning direction and twinning plane can be easily determined to be $[3\bar{3}2]$ and $(1\bar{1}2)$ from the geometrical relation between the Zr_2Fe

matrix phase and rotation twin [23]. Based on the above analyses, the crystallographic relationship between Zr_2Fe matrix phase and rotation twin was simulated, as shown in Fig. 6b.

Conclusion

The intermetallic phases in the Zr-4 alloy have been identified as C16-type Zr_2Fe with a body-centered tetragonal structure. Streaks, which either penetrate through the whole grain or the terminated inside, were frequently observed and determined to be stacking faults and micro growth twins, respectively. Atomic-scale investigations show that the stacking faults plane and displacement vector are (110) plane and $1/4[1\bar{1}1]$, respectively. HRTEM analysis reveals that the intrinsic growth twins belong to 60° rotation twin with the rotation axis of $[1\bar{1}0]$ crystallographic direction. In addition, the corresponding twinning plane and direction were respectively determined to be $(1\bar{1}2)$ and $[3\bar{3}2]$ by employed geometric analysis method.

Acknowledgements

We authors thank Dr. Liu Jinmin for the TEM measurement.

Declarations

Conflict of interest We declare that we have no financial and personal relationships with other people or organizations that can inappropriately influence our work, there is no professional or other personal interest of any nature or kind in any product, service and/or company that could be construed as influencing the position presented in, or the review of, the manuscript entitled .

References

- [1] Cox B (2005) Some thoughts on the mechanisms of in-reactor corrosion of zirconium alloys. *J Nucl Mater* 336:331–368
- [2] Zhang J, Yang H, Liming T, Sun F, Yao M, Zhou B (2016) Corrosion behavior and oxide microstructure of Zr–1Nb–xGe alloys corroded in 360 °C/18.6 MPa deionized water. *Corros Sci* 102:161–167
- [3] Chen L, Li J, Zhang Y, Zhang L-C, Weijie Lu, Wang L, Zhang L, Zhang Di (2015) Zr–Sn–Nb–Fe–Si–O alloy for fuel cladding candidate: processing, microstructure, corrosion resistance and tensile behavior. *Corros Sci* 100:332–340
- [4] Yuan F, Li G, Han F, Zhang Y, Muhammad A, Guo W, Gu H (2020) Shear deformation behavior of Zircaloy-4 alloy plate. *Mater Sci Eng A* 774:138914
- [5] Han F, Liu C, Yuan F, Zhang Y, Ali M, Hengfei Gu, Li G (2019) Microscopic characterization on low cycle fatigue behavior at room temperature of Zircaloy-4 alloy with recrystallized microstructure. *J Alloy Compd* 778:318–326
- [6] Lumley SC, Murphy ST, Burr PA, Grimes RW, Chard-Tuckey PR, Wenman MR (2013) The stability of alloying additions in Zirconium. *J Nucl Mater* 437:122–129
- [7] Versaci RA, Ipohorski M (1979) polytype structure of intermetallic precipitates in Zircaloy-4 alloys. *J Nucl Mater* 80:180–183
- [8] Yuan F, Li G, Liu C, Han F, Zhang Y, Muhammad A, Gu H, Guo W, Ren J (2020) Cross stacking faults in Zr(Fe, Cr)₂ face-centered cubic Laves phase nanoparticle. *Appl Surface Sci* 513:145716
- [9] Cao G, Yun Y, Yang L, Yuan G, Yue Q, Shao G, Hua J (2017) The formation and stacking faults of Fe and Cr containing Laves phase in Zircaloy-4 alloy. *Mater Lett* 191:203–205
- [10] Liu C, Li G, Yuan F, Han F, Zhang Y, Hengfei Gu (2018) Stacking faults in Zr(Fe, Cr)₂ Laves structured secondary phase particle in Zircaloy-4 alloy. *Nanoscale* 10:2249–2254
- [11] Yuan F, Liu C, Han F, Zhang Y, Muhammad A, Guo W, Hengfei Gu, Li G (2020) Stress-induced C14→C15 phase transformation in a Zr(Fe, Cr)₂ Laves structured nanoparticle. *J Appl Crystallogr* 53:222–225
- [12] Jiang M, Oikawa K, Ikeshoji T, Wulff L, Ishida K (2001) Thermodynamic calculations of the Fe–Zr and Fe–Zr–C systems. *J Ph Equilib* 22:406–417
- [13] Degueldre C, Raabe J, Kuria G, Abolhassani S (2008) Zircaloy-2 secondary phase precipitate analysis by X-ray microspectroscopy. *Talanta* 75:402–406
- [14] Tao B, Qiu R, Zhao Y, Liu Y, Tan X, Luan B, Liu Q (2018) Effects of alloying elements (Sn, Cr and Cu) on second phase particles in Zr–Sn–Nb–Fe–(Cr, Cu) alloys. *J Alloy Compd* 748:745–757
- [15] Sayers J, Lozano-Perez S, Ortner SR (2019) The progress of SPP oxidation in Zircaloy-4 and its relation to corrosion and hydrogen pickup. *Corros Sci* 158:108072
- [16] Annand K, Nord M, MacLarena I, Gass M (2017) The corrosion of Zr(Fe, Cr)₂ and Zr₂Fe secondary phase particles in Zircaloy-4 under 350 °C pressurised water condition. *Corros Sci* 128:213–223

- [17] Wei C-C, Aitkaliyeva A, Luo Z, Ewh A, Sohn YH KJR, Sencer BH, Myers MT, Martin M, Wallace J, General MJ, Shao L (2013) Understanding the phase equilibrium and irradiation effects in Fe–Zr diffusion couples. *J Nuclear Mater* 432:205–211
- [18] Huang J, Yao MY, Gao CY et al (2015) The influence of second phase particles on the crack formation in oxides films formed on zirconium alloys. *Corros Sci* 99:172–177
- [19] Hatano Y, Hitaka R, Sugisaki M et al (1997) Influence of size distribution of $Zr(Fe, Cr)_2$ precipitates on hydrogen transport through oxide film of Zircaloy-4. *J Nuclear Mater* 248:311–314
- [20] Zhou Q, Wang J, Misra A, Huang P, Wang F, Xu K (2016) Atomistic study of fundamental character and motion of dislocations in intermetallic Al_2Cu . *Int J Plast* 87:100–113
- [21] Wang SJ, Liu G, Xie DY, Lei Q, Ramakrishnan BP, Mazumder J, Wang J, Misra A (2018) Plasticity of laser-processed nanoscale Al– Al_2Cu eutectic alloy. *Acta Mater* 156:52–63
- [22] Bonnet R, Loubradou M (2002) Crystalline defects in a B.C.T. Al_2Cu θ single crystal obtained by unidirectional solidification along [001]. *Phys Stat Solidi (A) Appl Res* 194(1):173–191
- [23] Yuan F, Li G, Han F, Zhang Y, Ali M, Guo W, JieRen CL, Hengfei G (2021) Rotation twin in body-centered tetragonal $SiZr_2$ nanoparticle in silicon modified Zircaloy-4 alloy. *J Alloys Compd* 862:158386
- [24] Hu X, Zhu YL, Ma XL (2014) Crystallographic account of nano-scaled intergrowth of M2B-type borides in nickel-based superalloys. *Acta Mater* 68(15):70–81
- [25] Feng ZQ, Yang Y, Huang B, Li M, Chen Y, Ru JG (2014) Crystal substructures of the rotation-twinned T ($Al_{20}Cu_{2}Mn_3$) phase in 2024 aluminum alloy. *J Alloys Compd* 583:445–451
- [26] Zandbergen HW, van den Berg J, Kes PH (1990) Flux pinning of (100) mirror twin boundaries and 90° rotation twin boundaries in $YBaCu_3O_{7-\delta}$. *Cryogenics* 30:633–638

Publisher's Note Springer Nature remains neutral with regard to jurisdictional claims in published maps and institutional affiliations.